

Viscous Flow Solvers for Aero/Hydrodynamic Analysis and Design

LUIGI MARTINELLI*

Department of Mechanical & Aerospace Engineering
Princeton University
Princeton, NJ 08544, USA

ANTONY JAMESON†

Department of Aeronautics & Astronautics
Stanford University
Stanford, California 94305 USA

ABSTRACT

This paper reviews the principles underlying the development of numerical techniques for the solution of both steady and time dependent viscous flow problems. The combination of efficient high resolution schemes and parallel computing enables the effective use of viscous analyses in the preliminary stages of a design. Representative results, drawn by the authors work in several application areas, are presented.

INTRODUCTION

Most, if not all, major industrial applications of Computational Fluid Dynamics (CFD) ultimately require the simulation of three-dimensional viscous flow at high Reynolds number. Thus, pursuing the development of advanced simulation tools for this class of flow has been, and still is, of great importance. Despite the advances that have been made in the last fifteen years, the simulation of high Reynolds number flow is still a challenging task and is not being exploited as effectively as one would like in the design process. Besides the endemic difficulties of turbulence modeling, the fidelity of modeling of high Reynolds number viscous flows continues to be limited by computational costs. Even on a simple three-dimensional wing mesh-resolved three dimensional calculations at transonic speed using the Reynolds Averaged Navier-Stokes Equations (RANS) may require meshes with as many as 5–10 million cells = 8,388,608 cells. A typical algorithm requires of the order of 5,000 floating point

operations per mesh point in one multigrid iteration. With 10 million mesh points, the operation count is of the order of 0.5×10^{11} per cycle. Given a computer capable of sustaining 10^9 operations per second (1 gigaflop), 200 cycles require approximately 10,000 seconds, that makes this kind of calculations still a bit too expensive. Simulations of unsteady viscous flows (flutter, buffet) are likely to require 1,000–10,000 time steps. A further progression to large eddy simulation of complex configurations requires even greater resources. Consequently accurate and cost effective simulation of viscous flow at Reynolds numbers associated with full scale flight, such as the prediction of high lift devices, remains a challenge, and there remains a compelling need of improving both the efficiency and accuracy of viscous solvers.

The development over the past few years of a comprehensive theoretical framework for shape optimization, has opened new possibilities for exploiting CFD in design. However, practical implementation of the viscous design method based on control theory [1, 2] for complex configurations relies heavily upon fast and accurate solvers for both the state and co-state systems. This again suggests and justifies efforts to improve the present generation of solvers.

Several routes are available toward the reduction of computational costs, including the reduction of mesh requirements by the use of higher order schemes, improved convergence to a steady state by sophisticated acceleration methods, fast inversion methods for implicit schemes for the simulation of time dependent flow, and the exploitation of massively parallel computers.

This paper reviews the principles underlying the de-

*AIAA Member, Assistant Professor

†AIAA Fellow, T. V. Jones Professor of Engineering

Copyright ©1998 by the Authors.

Published by the AIAA Inc. with permission

velopment of numerical techniques for the solution of both steady and time dependent viscous flow problems. Its only intent is to summarize some of the activities of the authors in the area of viscous flow simulation. Representative results, drawn by the authors work in several application areas, are presented to outline capabilities as well as deficiencies of current viscous flow solvers.

NAVIER-STOKES EQUATIONS

In Cartesian coordinates (x_1, x_2, x_3) and by adopting the indicial notation where a repeated index "i" implies summation over $i = 1$ to 3, the three-dimensional compressible Navier-Stokes equations take the form

$$\frac{\partial w}{\partial t} + \frac{\partial f_i}{\partial x_i} = \frac{\partial f_{vi}}{\partial x_i} \quad \text{in } \mathcal{D}, \quad (1)$$

where the state vector w , inviscid flux vector f and viscous flux vector f_v are described respectively by

$$w = \begin{Bmatrix} \rho \\ \rho u_1 \\ \rho u_2 \\ \rho u_3 \\ \rho E \end{Bmatrix}, \quad (2)$$

$$f_i = \begin{Bmatrix} \rho u_i \\ \rho u_i u_1 + p \delta_{i1} \\ \rho u_i u_2 + p \delta_{i2} \\ \rho u_i u_3 + p \delta_{i3} \\ \rho u_i H \end{Bmatrix}, \quad (3)$$

$$f_{vi} = \begin{Bmatrix} 0 \\ \sigma_{ij} \delta_{j1} \\ \sigma_{ij} \delta_{j2} \\ \sigma_{ij} \delta_{j3} \\ u_j \sigma_{ij} + k \frac{\partial T}{\partial x_i} \end{Bmatrix}. \quad (4)$$

In these definitions, ρ is the density, u_1, u_2, u_3 are the Cartesian velocity components, E is the total energy and δ_{ij} is the Kronecker delta function. The pressure is determined by the equation of state

$$p = (\gamma - 1) \rho \left\{ E - \frac{1}{2} (u_i u_i) \right\},$$

and the stagnation enthalpy is given by

$$H = E + \frac{p}{\rho},$$

where γ is the ratio of the specific heats. The viscous stresses may be written as

$$\sigma_{ij} = \mu \left(\frac{\partial u_i}{\partial x_j} + \frac{\partial u_j}{\partial x_i} \right) + \lambda \delta_{ij} \frac{\partial u_k}{\partial x_k}, \quad (5)$$

where μ and λ are the first and second coefficients of viscosity. The coefficient of thermal conductivity and the temperature are computed as

$$k = \frac{c_p \mu}{Pr}, \quad T = \frac{p}{R\rho}, \quad (6)$$

where Pr is the Prandtl number, c_p is the specific heat at constant pressure, and R is the gas constant.

For discretization on a body conforming structured mesh, it is also useful to consider a transformation to the computational coordinates (ξ_1, ξ_2, ξ_3) defined by the metrics

$$K_{ij} = \left[\frac{\partial x_i}{\partial \xi_j} \right], \quad J = \det(K), \quad K_{ij}^{-1} = \left[\frac{\partial \xi_i}{\partial x_j} \right].$$

The Navier-Stokes equations can then be written in computational space as

$$\frac{\partial (Jw)}{\partial t} + \frac{\partial (F_i - F_{vi})}{\partial \xi_i} = 0 \quad \text{in } \mathcal{D}, \quad (7)$$

where the inviscid and viscous flux contributions are now defined with respect to the computational cell faces by $F_i = S_{ij} f_j$ and $F_{vi} = S_{ij} f_{vj}$, and the quantity $S_{ij} = JK_{ij}^{-1}$ represents the projection of the ξ_i cell face along the x_j axis. In obtaining equation (7) we have made use of the property that

$$\frac{\partial S_{ij}}{\partial \xi_i} = 0 \quad (8)$$

which represents the fact that the sum of the face areas over a closed volume is zero, as can be readily verified by a direct examination of the metric terms. It is well known that by Reynolds averaging the equations one obtains a set of partial differential equations for the mean flow that closely resembles the Navier-Stokes equations except for the inclusion of the Reynolds stress tensor which requires additional modeling. Thus, discretizations of the Navier-Stokes equations are easily extended to the Reynolds Averaged Equations (RANS) provided that a suitable turbulence model is implemented for closure.

DISCRETIZATION

The discretization of the spatial operators is accomplished by using a finite volume method, both cell centered and vertex base schemes have been developed over a period of fifteen years. The flow domain is divided into a large number of small subdomains, and the integral form of the conservation laws

$$\frac{\partial}{\partial t} \int_{\mathcal{D}} \mathbf{w} dV + \int_{\mathcal{B}} \mathbf{F} \cdot d\mathbf{S} = 0$$

is applied to each subdomain. Here \mathbf{F} is the flux appearing in equation (7) and $d\mathbf{S}$ is the directed surface element of the boundary \mathcal{B} of the domain \mathcal{D} .

The use of the integral form has the advantage that no assumption of the differentiability of the solution is implied, with the result that it remains a valid statement for a subdomain containing a shock wave. In general the subdomains could be arbitrary, but in this work we use the hexahedral cells of a body-conforming curvilinear mesh.

To include the viscous terms of the Navier-Stokes equations into the spatial discretization scheme it is necessary to approximate the velocity derivatives $\frac{\partial u_i}{\partial x_j}$ which constitute the stress tensor σ_{ij} . These derivatives may be evaluated by applying Gauss' formula to a control volume V with boundary S :

$$\int_V \frac{\partial u_i}{\partial x_j} dV = \int_S u_i n_j dS,$$

where n_j is the outward normal. For a hexahedral cell this gives

$$\overline{\frac{\partial u_i}{\partial x_j}} = \frac{1}{V} \sum_{\text{faces}} \bar{u}_i n_j S, \quad (9)$$

where \bar{u}_i is an estimate of the average of u_i over the face, n_j is the j -th component of the normal, and S is the face area.

Discretizations of this type reduce to central differences on a regular Cartesian grid, and in order to eliminate possible odd-even decoupling modes allowed by the discretization of the convective terms some form of artificial dissipation must be added. Moreover, when shock waves are present, it is necessary to upwind the discretization to provide a non-oscillatory capture of discontinuities. The effects of numerical diffusion, which may be introduced either explicitly to avoid decoupling or implicitly by means of upwind formulas, could adversely impact the overall accuracy of the solution. Thus, extreme care in devising an appropriate numerical diffusion, or upwind method is required. The next section gives some details on the baseline formulation currently implemented in our solvers.

UPWINDING AND NUMERICAL VISCOSITY

In the past few years, we have analyzed a large class of schemes including High Resolution Switched schemes, Symmetric Limited Positive (SLIP) and Upstream Limited Positive (USLIP) schemes [3, 4]. SLIP and USLIP schemes were implemented and tested using several forms of flux-splitting including scalar, characteristic, and Convective Upstream Split Pressure (CUSP) schemes. Careful comparisons with analytical results for laminar boundary layers [5] clearly indicate that the limiting process plays a greater role than the flux-splitting in determining the quality of viscous results. However,

new trade-offs between the different forms of flux-splitting arise whenever crisp resolution of shocks becomes important.

Roe has shown that characteristic splitting can yield an optimal discrete shock resolution with only one interior point [6]. More recently Jameson [7] has shown that a discrete shock structure with a single interior point can, in general, be supported by artificial diffusion which both:

1. produces an upwind flux if the flow is determined to be supersonic through the interface between the left and the intermediate state,
2. satisfies a generalized eigenvalue problem for the exit from the shock.

These two conditions can be satisfied by both the characteristic and CUSP schemes whereas scalar diffusion fails to satisfy the first condition.

At this time CUSP based schemes which combine perfect one-point shock capturing of stationary shocks with high resolution of boundary layers, are considered to be the best compromise.

For simplicity we consider only the general one dimensional conservation law for a system of equations which can be expressed as

$$\frac{\partial w}{\partial t} + \frac{\partial}{\partial x} f(w) = 0. \quad (10)$$

Here the state and the flux vectors are

$$w = \begin{pmatrix} \rho \\ \rho u \\ \rho E \end{pmatrix}, \quad f = \begin{pmatrix} \rho u \\ \rho u^2 + p \\ \rho u H \end{pmatrix},$$

where ρ is the density, u is the velocity, E is the total energy, p is the pressure, and H is the stagnation enthalpy. If γ is the ratio of specific heats and c is the speed of sound then

$$p = (\gamma - 1)\rho \left(E - \frac{u^2}{2} \right)$$

$$c^2 = \frac{\gamma p}{\rho}$$

$$H = E + \frac{p}{\rho} = \frac{c^2}{\gamma - 1} + \frac{u^2}{2}.$$

In a steady flow H is constant. This remains true for the discrete scheme only if the numerical diffusion is constructed so that it is compatible with this condition.

It is well known that when the flow is smooth it can be represented by the quasi-linear form

$$\frac{\partial w}{\partial t} + A(w) \frac{\partial w}{\partial x} = 0,$$

where $A(w) = \frac{\partial f}{\partial w}$, and the eigenvalues u , $u + c$ and $u - c$ of the Jacobian matrix A are the wave speeds for the three characteristics. Depending on the initial data, there may not be a smooth solution of the conservation law (10). Nonlinear wave interactions along converging characteristics may lead to the formation and propagation of shock waves, while contact discontinuities may also appear.

The conservation law (10) is approximated over the interval $(0, L)$ on a mesh with an interval Δx by the semi-discrete scheme

$$\Delta x \frac{dw_j}{dt} + h_{j+\frac{1}{2}} - h_{j-\frac{1}{2}} = 0, \quad (11)$$

where w_j denotes the value of the discrete solution in cell j , and $h_{j+\frac{1}{2}}$ is the numerical flux between cells j and $j + 1$.

The numerical flux can be taken as

$$h_{j+\frac{1}{2}} = \frac{1}{2}(f_{j+1} + f_j) - d_{j+\frac{1}{2}}, \quad (12)$$

where f_j denotes the flux vector $f(w_j)$ evaluated for the state w_j , and $d_{j+\frac{1}{2}}$ is a diffusive flux which is introduced to enable the scheme to resolve discontinuities without producing oscillations in the discrete solution.

A rather general form for the diffusive flux is

$$d_{j+\frac{1}{2}} = \frac{1}{2}\alpha_{j+\frac{1}{2}}B_{j+\frac{1}{2}}(w_{j+1} - w_j),$$

where the matrix $B_{j+\frac{1}{2}}$ controls the numerical diffusion and determines the properties of the scheme, and the scaling factor $\alpha_{j+\frac{1}{2}}$ is included for convenience. Notice that since $w_{j+1} - w_j$ approximates $\Delta x \frac{\partial w}{\partial x}$, the diffusive flux introduces an error proportional to the mesh width, whence, all these schemes will be first order accurate unless compensating anti-diffusive terms are introduced.

With this notation, scalar diffusion is produced by setting

$$B_{j+\frac{1}{2}} = I, \quad (13)$$

while the characteristic upwind scheme is produced by setting

$$B_{j+\frac{1}{2}} = \left| A_{j+\frac{1}{2}} \right| = T |\Lambda| T^{-1}. \quad (14)$$

In equation (14), $A_{j+\frac{1}{2}}(w_{j+1}, w_j)$ is an estimate of the Jacobian matrix $\frac{\partial f}{\partial w}$ obtained by Roe linearization, with the property that the equation

$$f_{j+1} - f_j = A_{j+\frac{1}{2}}(w_{j+1} - w_j)$$

is satisfied exactly, and T is a similarity transformation such that

$$A_{j+\frac{1}{2}} = T \Lambda T^{-1}. \quad (15)$$

Thus, the columns of T are the eigenvectors of $A_{j+\frac{1}{2}}$, and Λ is a diagonal matrix containing its eigenvalues. The symbol $\left| A_{j+\frac{1}{2}} \right|$ is used to represent the matrix obtained by replacing the eigenvalues by their absolute values.

An intermediate class of schemes which can be formulated by defining the first order diffusive flux as a combination of differences of the state and flux vectors

$$d_{j+\frac{1}{2}} = \frac{1}{2}\alpha_{j+\frac{1}{2}}^* c (w_{j+1} - w_j) + \frac{1}{2}\beta_{j+\frac{1}{2}} (f_{j+1} - f_j). \quad (16)$$

where the factor c is included so that α^* is dimensionless. Schemes of this class are fully upwind in supersonic flow if one takes $\alpha_{j+\frac{1}{2}} = 0$ and $\beta_{j+\frac{1}{2}} = \text{sign}(M)$ when the absolute value of the local Mach number satisfies $|M| > 1$. In order to support a stationary discrete shock structure with a single interior point, α^* and β cannot be chosen independently. It turns out that once α^* is chosen, β is uniquely determined by the equilibrium at the exit of the shock, leading to a one parameter family of schemes satisfying the relation

$$\alpha^* = (1 + \beta)(1 - M)$$

when $M > 0$ [7].

CUSP Formulation

Very accurate schemes of this class can be based on a decomposition of the flux vector f obtained by setting

$$f = uw + f_p, \quad (17)$$

where

$$f_p = \begin{pmatrix} 0 \\ p \\ up \end{pmatrix}. \quad (18)$$

Then

$$f_{j+1} - f_j = \bar{u}(w_{j+1} - w_j) + \bar{w}(u_{j+1} - u_j) + f_{p_{j+1}} - f_{p_j}, \quad (19)$$

where \bar{u} and \bar{w} are the arithmetic averages

$$\bar{u} = \frac{1}{2}(u_{j+1} + u_j), \quad \bar{w} = \frac{1}{2}(w_{j+1} + w_j).$$

If the convective terms are separated by splitting the flux according to equations (17), (18) and (19), then the total effective coefficient of convective diffusion is

$$\alpha c = \alpha^* c + \beta \bar{u}.$$

The choice $\alpha c = \bar{u}$ leads to low diffusion near a stagnation point, and also leads to a smooth continuation of convective diffusion across the sonic line since $\alpha^* = 0$ and $\beta = 1$ when $|M| > 1$. The scheme must

also be formulated so that the cases of $u > 0$ and $u < 0$ are treated symmetrically. Using the notation $M = \frac{u}{c}$, $\lambda^\pm = u \pm c$, this leads to the diffusion coefficients

$$\alpha = |M| \quad (20)$$

$$\beta = \begin{cases} + \max\left(0, \frac{u+\lambda^-}{u-\lambda^-}\right) & \text{if } 0 \leq M \leq 1 \\ - \max\left(0, \frac{u+\lambda^+}{u-\lambda^+}\right) & \text{if } -1 \leq M \leq 0 \\ \text{sign}(M) & \text{if } |M| \geq 1. \end{cases} \quad (21)$$

Near a stagnation point α may be modified to $\alpha = \frac{1}{2} \left(\alpha_0 + \frac{|M|^2}{\alpha_0} \right)$ if $|M|$ is smaller than a threshold α_0 . The expression for β in subsonic flow can also be expressed as

$$\beta = \begin{cases} \max(0, 2M - 1) & \text{if } 0 \leq M \leq 1 \\ \min(0, 2M + 1) & \text{if } -1 \leq M \leq 0 \end{cases}$$

Equation (21) remains valid when the CUSP scheme is modified as described below to allow solutions with constant stagnation enthalpy. The coefficients $\alpha(M)$ and $\beta(M)$ are displayed in figure 1 for the case when $\alpha_0 = 0$. The cutoff of β when $|M| < \frac{1}{2}$,

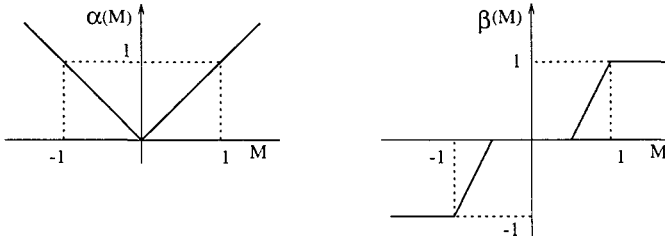


Figure 1: Diffusion Coefficients.

together with α approaching zero as $|M|$ approaches zero, is also appropriate for the capture of contact discontinuities.

An important property of this scheme can be illustrated by introducing a Roe linearization and by rewriting the diffusive flux as

$$d_{j+\frac{1}{2}} = \frac{1}{2} \left(\alpha^* c I + \beta A_{j+\frac{1}{2}} \right) (w_{j+1} - w_j).$$

Introducing the characteristic decomposition (15), the diffusive flux can now be represented as

$$d_{j+\frac{1}{2}} = R M R^{-1} (w_{j+1} - w_j)$$

The matrix M is diagonal with eigenvalues $\mu_1 c, \mu_2 c, \mu_3 c$ given by

$$\mu_1 = \alpha - \beta M + \beta M = \alpha = |M|$$

$$\mu_2 = \begin{cases} |M| & \text{if } |M| < \frac{1}{2} \\ \alpha + \beta & \text{if } \frac{1}{2} \leq M \leq 1 \\ |M + 1| & \text{if } |M| \geq 1 \end{cases}$$

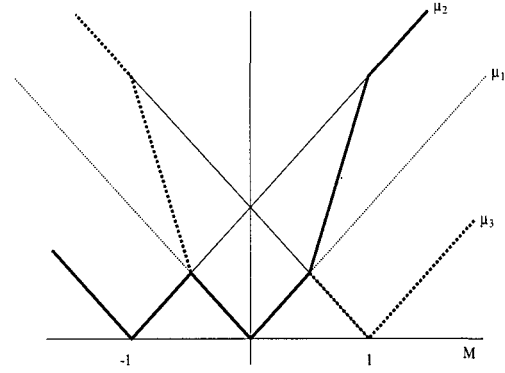


Figure 2: Eigenvalues of diffusion matrix

$$\mu_3 = \begin{cases} |M| & \text{if } |M| < \frac{1}{2} \\ \alpha - \beta & \text{if } \frac{1}{2} \leq M \leq 1 \\ |M - 1| & \text{if } |M| \geq 1 \end{cases}$$

These values are displayed in figure 2.

In the region $|M| \leq \frac{1}{2}$, $\mu_1 = \mu_2 = \mu_3 = |M|$, while in the region $|M| < 1$ $\mu_2 < |M+1|$, $\mu_3 < |M-1|$. Thus the scheme has lower diffusion than the standard characteristic upwind scheme. Strict positivity is not enforced, but at a shock

$$\Delta f = A \Delta w = S \Delta w$$

where S is the shock speed. Thus Δw must be an eigenvector corresponding to one of the eigenvalues $u \pm c$, and positivity is enforced for the corresponding characteristic variable.

In steady flow the stagnation enthalpy H is constant, corresponding to the fact that the energy and mass equations are consistent when the constant factor H is removed from the energy equation. Discrete and semi-discrete schemes do not necessarily satisfy this property. In the case of a semi-discrete scheme expressed in viscosity form - equations (11) and (12) - a solution with constant H is admitted if the viscosity for the energy equation reduces to the viscosity for the continuity equation with ρ replaced by ρH .

In order to extend the CUSP formulation to allow for isenthalpic solutions, we introduce the linearization

$$f_R - f_L = A_h (w_{hR} - w_{hL}).$$

where w_h is a modified state vector with ρH replacing ρE . The matrix A_h may be calculated in the same way as the standard Roe linearization. In par-

ticular, by introducing the vector

$$v = \begin{pmatrix} \sqrt{\rho} \\ \sqrt{\rho}u \\ \sqrt{\rho}H \end{pmatrix},$$

all quantities in both f and w_h are products of the form $v_j v_k$ which have the property that a finite difference $\Delta(v_j v_k)$ between left and right states can be expressed as

$$\Delta(v_j v_k) = \bar{v}_j \Delta v_k + \bar{v}_k \Delta v_j$$

where \bar{v}_j is the arithmetic mean $\frac{1}{2}(v_{jR} + v_{jL})$. Therefore,

$$\Delta w = B \Delta v, \quad \Delta f = C \Delta v = C B^{-1} \Delta w,$$

where B and C can be expressed in terms of appropriate mean values of the quantities v_j . Thus, by defining

$$u = \frac{\sqrt{\rho_R} u_R + \sqrt{\rho_L} u_L}{\sqrt{\rho_R} + \sqrt{\rho_L}}, \quad H = \frac{\sqrt{\rho_R} H_R + \sqrt{\rho_L} H_L}{\sqrt{\rho_R} + \sqrt{\rho_L}},$$

and

$$c = \sqrt{(\gamma - 1)(H - \frac{u^2}{2})},$$

it follows that

$$A_h = \begin{pmatrix} 0 & 1 & 0 \\ -\frac{\gamma+1}{\gamma} \frac{u^2}{2} & \frac{\gamma+1}{\gamma} u & \frac{\gamma-1}{\gamma} \\ -uH & H & u \end{pmatrix}.$$

The eigenvalues of A_h are u , λ^+ and λ^- where

$$\lambda^\pm = \frac{\gamma+1}{2\gamma} u \pm \sqrt{\left(\frac{\gamma+1}{2\gamma} u\right)^2 + \frac{c^2 - u^2}{\gamma}}. \quad (22)$$

Note that λ^+ and λ^- have the same sign as $u + c$ and $u - c$, and change sign at the sonic line $u = \pm c$. The corresponding left and right eigenvectors of A_h can be computed, and are given in [7].

Using the modified linearization the CUSP scheme can be reformulated as follows to admit isenthalpic steady solutions. The diffusive flux is expressed as

$$d_{j+\frac{1}{2}} = \frac{1}{2} \alpha^* c \Delta w_h + \frac{1}{2} \beta \Delta f,$$

where Δ denotes the difference from $j+1$ to j . The split is redefined as

$$f = u w_h + f_p,$$

where

$$f_p = \begin{pmatrix} 0 \\ p \\ 0 \end{pmatrix}$$

and the diffusive flux can be expressed as

$$d_{j+\frac{1}{2}} = \frac{1}{2} \alpha c \Delta w_h + \frac{1}{2} \beta \bar{w}_h \Delta u + \frac{1}{2} \beta \Delta f_p.$$

As before, α and β are defined by equations (20) and (21), using the modified eigenvalues λ^\pm defined equation (22). This splitting corresponds to the Liou-Steffen splitting [8, 9], and in the remaining of this paper it will be denoted as H-CUSP formulation.

Implementation of Limiters

In the case of a scalar conservation law, high resolution schemes which guarantee the preservation of the positivity or monotonicity of the solution can be constructed by limiting the action of higher order or anti-diffusive terms, which might otherwise cause extrema to grow. Typically, these schemes, compare the slope of the solution at nearby mesh intervals. The fluxes appearing in the CUSP scheme have different slopes approaching from either side of the sonic line, and use of limiters which depends on comparisons of the slopes of these fluxes can lead to a loss of smoothness in the solution at the entrance to supersonic zones in the flow. This problem can be avoided in the implementation of the CUSP schemes by forming the diffusive flux from left and right states at the cell interface. These are interpolated or extrapolated from nearby data, subject to limiters to preserve monotonicity. In a similar manner to the reconstruction of the solution in Van Leer's MUSCL scheme [10], we use the following construction.

Define the limiter

$$R(u, v) = 1 - \left| \frac{u - v}{|u| + |v|} \right|^q, \quad (23)$$

where q is a positive power which is set equal to two in the present study. Clearly $R(u, v) = 0$ when u and v have opposite sign. Also define the limited average

$$L(u, v) = \frac{1}{2} R(u, v)(u + v). \quad (24)$$

Let $w^{(k)}$ denote the k th element of the state vector w . Now define left and right states for each dependent variable separately as

$$\begin{aligned} w_L^{(k)} &= w_j^{(k)} + \frac{1}{2} L(\Delta w_{j+\frac{3}{2}}^{(k)}, \Delta w_{j-\frac{1}{2}}^{(k)}) \\ w_R^{(k)} &= w_{j+1}^{(k)} - \frac{1}{2} L(\Delta w_{j+\frac{3}{2}}^{(k)}, \Delta w_{j-\frac{1}{2}}^{(k)}), \end{aligned}$$

where

$$\Delta w_{j+\frac{1}{2}} = w_{j+1} - w_j.$$

Then

$$w_R^{(k)} - w_L^{(k)} = \Delta w_{j+\frac{1}{2}}^{(k)} - L(\Delta w_{j+\frac{3}{2}}^{(k)}, \Delta w_{j-\frac{1}{2}}^{(k)})$$

which in the case of a scalar equation reduces to the SLIP formulation [11].

For the CUSP schemes the pressures p_L and p_R for the left and right states are determined from w_L and w_R . Then the diffusive flux is calculated by substituting w_L for w_j and w_R for w_{j+1} to give

$$d_{j+\frac{1}{2}} = \frac{1}{2}\alpha^*c(w_R - w_L) + \frac{1}{2}\beta(f(w_R) - f(w_L)).$$

The alternative reconstruction:

$$\begin{aligned} w_L^{(k)} &= w_j^{(k)} + R(\Delta w_{j+\frac{3}{2}}^{(k)}, \Delta w_{j-\frac{1}{2}}^{(k)})\Delta w_{j-\frac{1}{2}}^{(k)} \\ w_R^{(k)} &= w_j^{(k)} - R(\Delta w_{j+\frac{3}{2}}^{(k)}, \Delta w_{j-\frac{1}{2}}^{(k)})\Delta w_{j+\frac{3}{2}}^{(k)} \end{aligned}$$

has been found to yield essentially identical results for calculations of steady flows.

TIME STEPPING SCHEME

When the space discretization procedure is implemented separately from the discretization in time, it leads to a set of coupled ordinary differential equations which can be written in the form

$$\frac{d\mathbf{w}}{dt} + \mathbf{R}(\mathbf{w}) = \mathbf{0}, \quad (25)$$

where \mathbf{w} is the vector of the flow variables at the mesh locations, and $\mathbf{R}(\mathbf{w})$ is the vector of the residuals, consisting of the flux balances defined by the spatial discretization together with the added dissipative terms. If the objective is simply to reach the steady state and details of the transient solution are immaterial, the time-stepping scheme may be designed solely to maximize the rate of convergence.

Throughout this work we use a multistage explicit scheme, belonging to the general class of Runge-Kutta schemes [12]. Schemes of this type have proved very effective for a wide variety of problems, and they have the advantage that they can be applied equally easily on both structured and unstructured meshes [13, 14, 15, 16, 17].

If one reduces the linear scalar model problem corresponding to (25) to an ordinary differential equation by substituting a Fourier mode $\hat{w} = e^{ipx_j}$, the resulting Fourier symbol has an imaginary part proportional to the wave speed, and a negative real part proportional to the diffusion. Thus, the time stepping scheme should have a stability region which contains a substantial interval of the negative real axis, as well as an interval along the imaginary axis. To achieve this we treat the convective and dissipative terms in a distinct fashion. Thus, the residual is split as

$$R(w) = Q(w) + D(w),$$

where $Q(w)$ is the convective part and $D(w)$ the dissipative part. Denote the time level $n\Delta t$ by a

superscript n . Then the multistage time stepping scheme is formulated as

$$\begin{aligned} w^{(n+1,0)} &= w^n \\ &\dots \\ w^{(n+1,k)} &= w^n - \alpha_k \Delta t \left(Q^{(k-1)} + D^{(k-1)} \right) \\ &\dots \\ w^{n+1} &= w^{(n+1,m)}, \end{aligned}$$

where the superscript k denotes the k -th stage, $\alpha_m = 1$, and

$$\begin{aligned} Q^{(0)} &= Q(w^n), \quad D^{(0)} = D(w^n) \\ &\dots \\ Q^{(k)} &= Q(w^{(n+1,k)}) \\ D^{(k)} &= \beta_k D(w^{(n+1,k)}) + (1 - \beta_k)D^{(k-1)}. \end{aligned}$$

The coefficients α_k are chosen to maximize the stability interval along the imaginary axis, and the coefficients β_k are chosen to increase the stability interval along the negative real axis.

The coefficients of a five-stage scheme [18] which has been found to be particularly effective are tabulated below.

$$\begin{aligned} \alpha_1 &= \frac{1}{4} & \beta_1 &= 1 \\ \alpha_2 &= \frac{1}{6} & \beta_2 &= 0 \\ \alpha_3 &= \frac{1}{6} & \beta_3 &= 0.56 \\ \alpha_4 &= \frac{1}{2} & \beta_4 &= 0 \\ \alpha_5 &= 1 & \beta_5 &= 0.44 \end{aligned} \quad (26)$$

CONVERGENCE ACCELERATION

Radical improvements in the rate of convergence to a steady-state solution can be realized by the multigrid time-stepping technique. The concept of acceleration by the introduction of multiple grids was first proposed by Fedorenko [19]. There is by now a fairly well-developed theory of multigrid methods for elliptic equations based on treating the updating scheme as a smoothing operator on each grid [20, 21]. This theory, however, does not hold for hyperbolic systems. Nevertheless, it seems that it ought to be possible to accelerate the evolution of a hyperbolic system to a steady state by using large time steps on coarse grids so that disturbances can be more rapidly expelled through the outer boundary. Various multigrid time-stepping schemes designed to take advantage of this effect have been proposed [22, 23, 24, 25, 26, 27, 28, 29, 30].

In our work we implement a multigrid scheme, originally developed by Jameson [23] for the Euler equations. This method uses a sequence of coarser meshes generated by eliminating alternate points in each coordinate direction. In order to give a precise description of the multigrid scheme, subscripts may

be used to indicate the grid level. Several transfer operations need to be defined. First the solution vector on grid k must be initialized as

$$w_k^{(0)} = T_{k,k-1} w_{k-1},$$

where w_{k-1} is the current value on grid $k-1$, and $T_{k,k-1}$ is a transfer operator. Next it is necessary to transfer a residual forcing function such that the solution on grid k is driven by the residuals calculated on grid $k-1$. This can be accomplished by setting

$$P_k = Q_{k,k-1} R_{k-1}(w_{k-1}) - R_k[w_k^{(0)}],$$

where $Q_{k,k-1}$ is another transfer operator. Then $R_k(w_k)$ is replaced by $R_k(w_k) + P_k$ in the time-stepping scheme. Thus, the multistage scheme is reformulated as

$$\begin{aligned} w_k^{(1)} &= w_k^{(0)} - \alpha_1 \Delta t_k [R_k^{(0)} + P_k] \\ \dots &\dots \\ w_k^{(q+1)} &= w_k^{(0)} - \alpha_{q+1} \Delta t_k [R_k^{(q)} + P_k]. \end{aligned}$$

The result $w_k^{(m)}$ then provides the initial data for grid $k+1$. Finally, the accumulated correction on grid k has to be transferred back to grid $k-1$ with the aid of an interpolation operator $I_{k-1,k}$. With properly optimized coefficients, multistage time-stepping schemes can be very efficient drivers of the multigrid process. A W -cycle of the type illustrated in Figure 3 proves to be a particularly effective strategy for managing the work split between the meshes. In a three-dimensional case the number of cells is reduced by a factor of eight on each coarser grid. On examination of the figure, it can therefore be seen that the work measured in units corresponding to a step on the fine grid is of the order of

$$1 + 2/8 + 4/64 + \dots < 4/3,$$

and consequently the very large effective time step of the complete cycle costs only slightly more than a single time step in the fine grid.

For turbulent calculations on the highly stretched meshes which are required for resolving boundary layers and wakes, a breakdown in asymptotic convergence rate of the multigrid time-stepping scheme is often observed. The two fundamental causes for multigrid performance degradation are stiffness in the discrete system and decoupling of modes in one or more coordinate direction. Way to circumvent these problems have been studied by Allmaras [31], Pierce [32, 33], Venkatakrishnan [34], and Mavriplis [35] among others. One preconditioned multigrid method which has been shown to perform well on three-dimensional calculation on highly stretched grids is based on a point-implicit block-Jacobi preconditioner with J-coarsening [33].

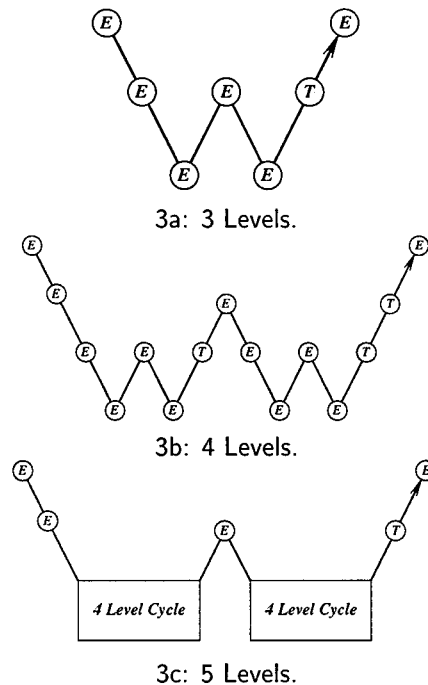


Figure 3: Multigrid W -cycle for managing the grid calculation. E , evaluate the change in the flow for one step; T , transfer the data without updating the solution.

The computational savings over the standard full-coarsened multigrid are roughly one order of magnitude to achieve convergence within engineering accuracy, and much larger in terms of asymptotic convergence rate. Nevertheless, these methods do not appear to be very robust as yet, and their success in practical applications depends on the quality of the computational mesh. In particular they tend to be highly responsive to mesh singularities which are almost unavoidable in practical applications. Thus, more research on the interaction of preconditioned multigrid methods and mesh quality is needed, before these techniques become of widespread use.

SOFTWARE IMPLEMENTATION

The explicit nature of the multigrid time-stepping scheme makes it suitable for efficient implementation on parallel computers. The parallelization strategy of choice developed in collaboration with J. Alonso [36] uses a domain decomposition model, a SPMD (Single Program Multiple Data) approach, and the MPI (Message Passing Interface) Library for message passing. The resulting codes are readily portable to different parallel computing platforms as well as to homogeneous and heterogeneous networks of workstations.

Communication between subdomains is performed through halo cells surrounding each subdomain

boundary. Since both the convective and the viscous fluxes are calculated at the cell faces (boundaries of the control volumes), all six neighboring cells are necessary, thus requiring the existence of a single level halo for each processor in the parallel calculation. The calculation of the dissipative fluxes requires values from the twelve neighboring cells (two adjacent to each face). For each cell within a processor, Figure 4 shows which neighboring cells are required for the calculation of convective, viscous, and dissipative fluxes. For each processor, some of these cells will lie directly next to an interprocessor boundary, in which case the values of the flow variables residing in a different processor will be necessary to calculate the fluxes.

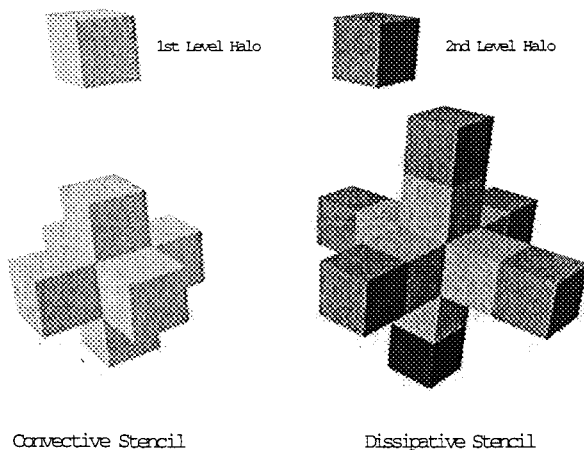


Figure 4: Convective and Dissipative Discretization Stencils.

The actual communication routines used are all of the asynchronous (or non-blocking) type. In the current implementation of the program, each processor must send and receive messages to and from at most 6 neighboring processors (left and right neighbors in each of the three coordinate directions). The communication is scheduled such that at every instant in time, pairs of processors are sending/receiving to/from one another in order to minimize contention in the communication schedule.

For problems with a low task granularity (ratio of the number of bytes received by a processor to the number of floating point operations it performs), large parallel efficiencies can be obtained. Current multigrid and implicit residual smoothing techniques are bound to hinder parallel performance for problems with smaller mesh sizes. For larger meshes used in viscous turbulent flow calculations on complete configurations, the granularity becomes low enough, and the parallel performance is quite high.

Several techniques can be applied to reduce the communication cost of the multigrid technique. Among

these, one can consider completely eliminating communication at the coarser levels of the multigrid cycle (thus allowing each processor to operate independently with the multigrid forcing terms at interprocessor boundaries derived from the flow variables in the finest mesh). Alternatively, one can also avoid sending messages at the end of every stage in the Runge-Kutta time stepping. Past experience has shown [37] that these savings in communication cost are usually offset by a degradation in the convergence rate of the overall algorithm. Therefore, in the present implementation we allow message passing any time the flow variables were altered.

STEADY AERODYNAMIC ANALYSIS

The first set of computations corresponds to the turbulent flow simulation on the ONERA-M6 wing at $M = 0.84$, $Re = 11.7$ million and $\alpha = 3.06^\circ$. The calculation was performed on a $193 \times 65 \times 49$ C-H grid using the vertex based formulation with the H-CUSP scheme. A Johnson and King turbulence model was adopted. Figure 5 shows the comparison of measured and computed pressure coefficients at four spanwise stations. The agreement with the experiments is quite reasonable, and the discrepancy at the station where the two branches of the typical transonic lambda shaped shock merge are to be expected from the limited spanwise resolution.

Routine use of RANS calculations of wing body configurations has become quite feasible in the preliminary stage of a design as it was demonstrated for example during the MDXX project in the summer of 1996. Using a parallel implementation of our own multiblock analysis program FLO107MB, which is one of the codes that implements the numerical methods described in this paper, we were able to complete a RANS analysis in a mesh with 1.5 - 2 million mesh cells in about $1 \frac{1}{2}$ hours using 32 processors of an IBM SP. This enabled us to evaluate the performance of 4 different candidate designs over the flight envelope with the aid of 60 Navier Stokes calculations over a weekend. The results allowed us to eliminate one design.

The RANS analysis of full aircraft configurations is still somewhat expensive. More because of human costs in grid generation than in actual computing costs. An example of the current capabilities is illustrated by the following computation which has been carried out by J. Reuther using FLO107MB for a transonic business jet configuration. The complete configuration is modeled, including the wing, body, nacelle, pylon, vertical tail, and horizontal tail. The mesh contains 240 blocks with 5.8 million cells including halos. It has the same general C-O topology with flow-through nacelles. For this calculation only

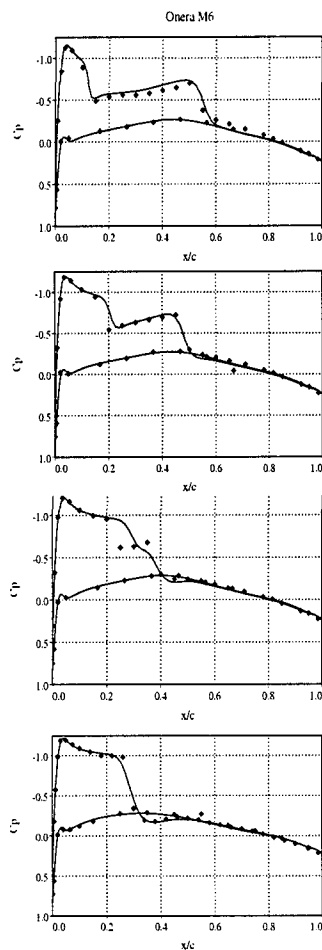


Figure 5: Comparison of Experimental and Computed Pressure Coefficients for the ONERA-M6 Wing. Spanwise Cuts at .44, .65, .80, .90 (Top to Bottom). $M = .84, Re = 11.7$ million, $\alpha = 3.06^\circ$.

the wing is treated with a no-slip boundary condition while the remaining solid surfaces are modeled as being inviscid. The wall normal spacing of the first cell was such that at the flight conditions a $y^+ = 1$ would be attained at the half span trailing edge assuming a flat plate turbulent boundary layer. At the flight conditions ($M = 0.80$ and an altitude of 40,000 ft) the Reynolds number is 1.45 million/ft. A Baldwin-Lomax turbulence model is used in the demonstration, which is adequate for this attached flow condition. Figure 6 shows the iso- C_P solution at $M = 0.82$, $Re = 1.45$ million/ft and $C_L = 0.36$. These results were obtained in 300 four-level multigrid cycles using 32 processors on an IBM SP. The reduction in the average residual was 4.3 orders and the elapsed wall time was 3.25 hours.

Vortex dominated flows are important for military aircraft and present a challenge for any viscous solver. They represent a very important testing ground not only for possible interferences of shock

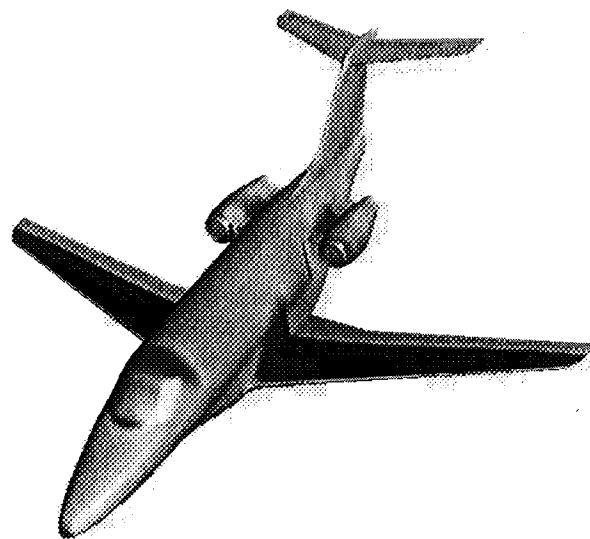


Figure 6: Business Jet Configuration. Iso- C_P Navier-Stokes solution with 240 blocks and 5.8 million mesh points. $M = 0.82, \alpha = 1.0^\circ$

capturing with an accurate resolution of boundary layers, but also for the effects that numerical viscosity may have on the transport of vorticity. A cropped delta wing with a sharp leading edge, allows to investigate these phenomena avoiding the inaccuracies which may arise from a poor simulation of the separation. The next set of computations corresponds to the turbulent flow simulation on a cropped delta wing wing at $M = 0.85$, $Re = 9$ million and $\alpha = 10^\circ$ [38]. The calculations were performed on a $193 \times 65 \times 96$ C-H grid using a vertex based formulation. Again the H-CUSP scheme was adopted in conjunction with a Johnson and King turbulence. Figure 7 shows a comparison of measured and computed pressure coefficients at three spanwise stations. It can be seen that the agreement is rather good, and the footprint of the primary vortex is at the right location, and the experimental pressure plateau in the outboard region is recovered. The vortical flow is visualized in Figure 8 by using iso-contours of total pressure. It should be noted that the vortical structures are captured very sharply by the H-CUSP scheme.

CHEMICALLY REACTIVE FLOW

The formulation described in this work has been extended to reactive flows in collaboration with Scott Sheffer. Reference [39] presents a detailed account of the extension required to implement the multigrid method for chemically reactive flows, as well as the results of a thorough validation study involving the

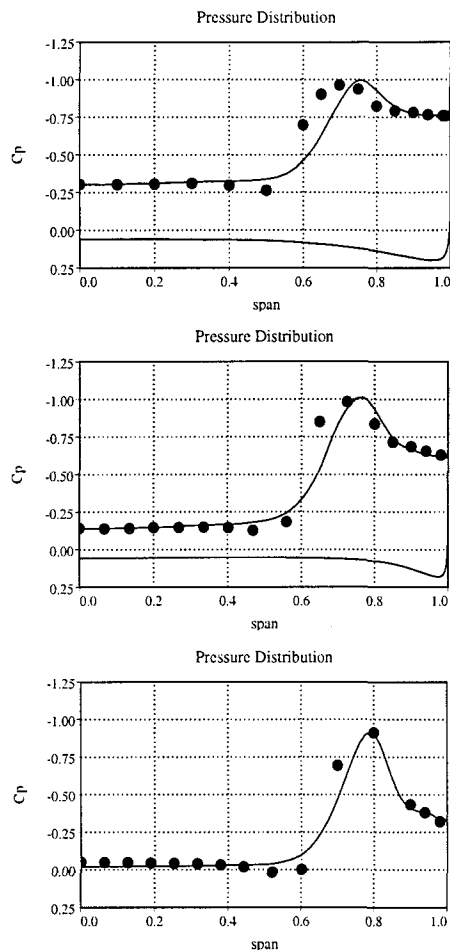


Figure 7: Comparison of Experimental and Computed Pressure Coefficients for a 65 deg Cropped Delta Wing. Chordwise Cuts at .6,.80,.967 (Top to Bottom). $M = .85, Re = 9\text{million}, \alpha = 10.0^\circ$.

comparison of computed results of inviscid and diffusive nonreactive and reactive flows with analytic or asymptotic solutions. The two results presented next illustrate the application of our method for the solution of steady compressible reactive flow with detailed chemistry.

Stoichiometric hydrogen/oxygen flow over an axisymmetric spherical tip projectile at $M = 3.55$ was simulated using the reduced chemistry model (six species, eight reactions) of Evans and Schexnayder [40]. This corresponds to an experiment conducted by Lehr [41]. The diameter of this projectile is 15 mm. The free stream temperature is 292 K and the free stream pressure is 24800 Pa. A simulation was performed on a 64×128 cell grid. Temperature contours for the simulation are presented in Figure 9 along with experimental shock and heat release front locations. Upon examination of Figure 9, it can be seen that the agreement between the computation and experiment is quite good. This computation

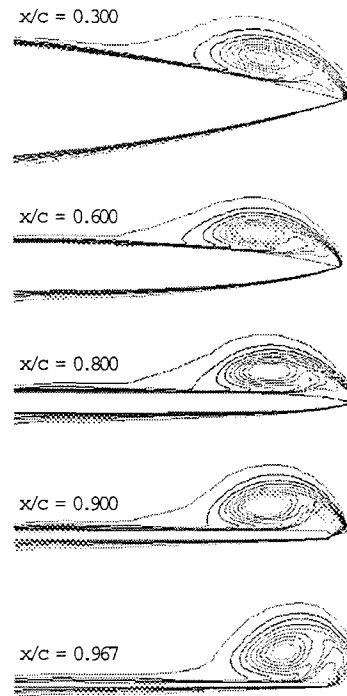


Figure 8: Iso-countours of Computed Total Pressure Coefficient for a 65 deg Cropped Delta Wing. Chordwise Cuts at .3,.6,.80,.9,.967 (Top to Bottom). $M = .85, Re = 9\text{million}, \alpha = 10.0^\circ$.

also agrees favorably with the simulation of Yungster *et al.* [42].

An additional test case consisted of a stoichiometric hydrogen/air flow over a 10° viscous ramp. The freestream Mach number was 4.0, the freestream temperature was 1200 K and the freestream pressure was one atmosphere. The 2 cm ramp was preceded by a 1 cm solid wall section. The effects of viscosity, heat conduction and species diffusion are all included in this computation. This is a common viscous/reactive test case, with several published computations available [43, 44, 45, 46] for turbulent reactive flows. However, because of the lack of concrete knowledge regarding the effect of turbulence on combustion, in this work the flow was computed assuming fully laminar flow. A grid convergence study was carried out to determine the accuracy and robustness of the numerical model. This flow was computed using Westbrook's nine species, seventeen reaction hydrogen/air mechanism because other researchers have applied such a model to this test case. This is a very challenging flow because of the myriad of physical phenomena that must be resolved accurately. The formation of the boundary layer must be captured well, without unnecessary dissipation, so that the displacement thickness is correct. The

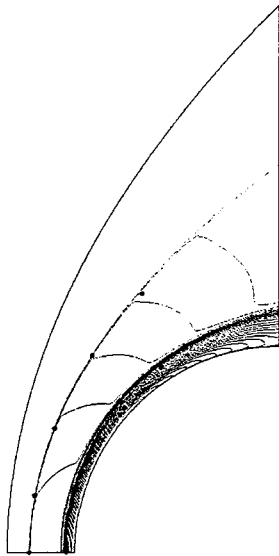


Figure 9: Temperature contours: $M = 3.55$ hydrogen/oxygen. Contour levels in K: min: 250, max: 3130, inc: 93. Grid size: 64×128 . Circles indicate experimental shock and heat release locations

conduction of heat must also be accurate so that the effects of viscous dissipation deep in the boundary layer are felt correctly in the sections of the boundary layer far from the wall. Proper resolution of the interaction of the shock and boundary layer and the oscillation free capture of the shock are essential, as is the correct modeling of species diffusion. The free stream temperature is not high enough to initiate a reaction, but the combination of high temperature in the boundary layer, diffusion of radicals in the direction normal to the wall and the oblique shock cause a reaction front to form past the shock in the ramp region.

Grid converged results were obtained for a 128×156 grid. Also, through a series of numerical experiments, it was determined that the computed results were insensitive to the location of the outflow boundary. The flow field temperature is depicted in Figure 10, and the curvature of the reaction front is an interesting phenomenon which was first observed on a truncated domain, and later verified using a larger domain of integration.

In this flow, radicals and heat in the boundary layer diffuse outward normal to the wall and eventually, along with the increased temperature and pressure behind the oblique shock, cause the reaction to proceed in the inviscid region behind the oblique shock. This reaction front couples with the shock toward the outflow plane and changes the angle of the discontinuity in the flow due to the pressure and heat release behind the shock/reaction front.

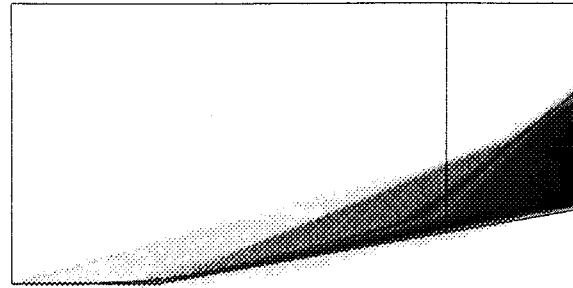


Figure 10: Temperature for extended domain: $M = 4.0$ hydrogen/air 10° viscous ramp, 128×156 grid. Temperature range: 1200–3500 K. Solid line in the computational domain indicates original outflow boundary.

FREE SURFACE FLOW

The numerical method described in this work has been extended also to compute free surface flow for hydrodynamic analysis of ships. Following a very standard procedure that is well documented in references [47, 48], the governing set of differential flow equations are expressed in the preconditioned form for artificial compressibility [49] as outlined by Rizzi and Eriksson [50]. The grid is allowed to adapt to the free surface movement by satisfying a kinematic condition which states that a fluid particle on the surface remains on the surface. The mesh adaptation allows to apply the dynamic free surface condition on the actual interface, so that no linearization is involved in the solution process.

Viscous calculations were performed on the Series 60 hullform for comparison with the experimental data from Iowa [51]. This rather simple hull is used to validate the code by comparison with both experiment and computations by other methods. Figures 11 and 12 show overhead wave contours and waterlines for both viscous and inviscid solutions of the Series 60 at Froude = .16.

Figures 13 and 14 show wave elevation contours and waterlines for the Series 60 hull at Froude = .316.

The Reynolds numbers for these calculations were 2 million and 4 million respectively, corresponding to the Iowa data. The grid spacing near the hull on the NS mesh is such that y^+ values in the first cell normal to hull reside in the range $.75 < y^+ < 1.5$.

A more complex configuration of a naval combatant (5415 Model) with a sonar dome and a transom stern is analyzed next. Figures 15 and 16 show overhead wave contours and waterlines for viscous and inviscid solutions of the model 5415 geometry at a Froude number of .2756 (20 Knots full scale). The Reynolds number was 12 million, corresponding to the test data taken at David Taylor Model Basin.

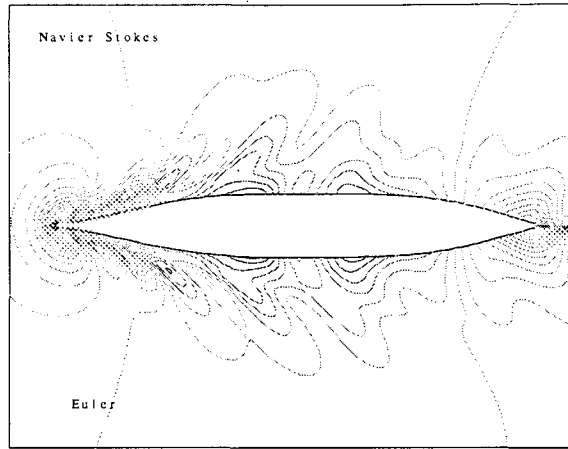


Figure 11: Overhead Wave Profiles: Series 60 (Fr = .16)

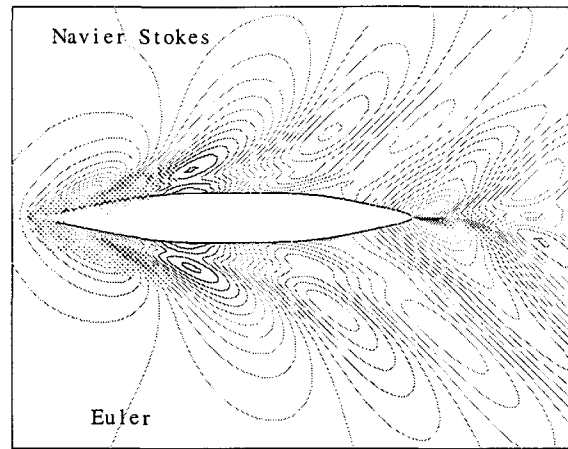


Figure 13: Overhead Wave Profiles: Series 60 (Fr = .316)

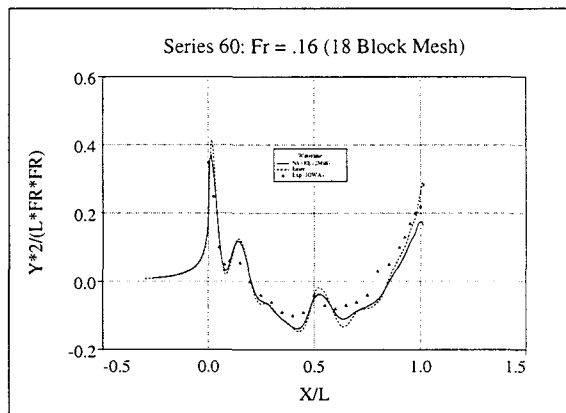


Figure 12: Comparison of Viscous and Inviscid Waterlines

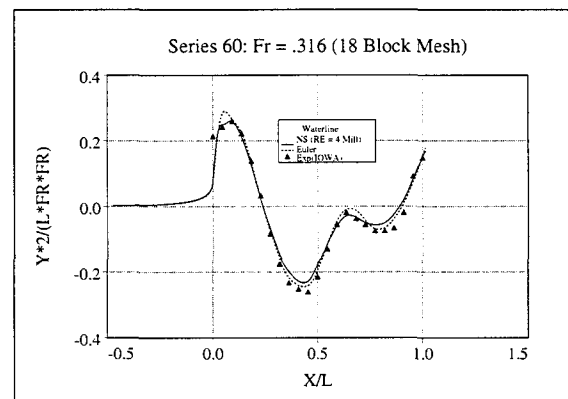


Figure 14: Comparison of Viscous and Inviscid Waterlines

Since the hullform has a transom stern, attempts to use a single structured block result in very skewed cells at the intersection of the and the symmetry plane aft of the boat. Thus a multiblock implementation with a second block fitted to the transom and extended to the outflow plane, is therefore more suitable for this geometry.

ADJOINT APPROACH TO OPTIMAL DESIGN

An adjoint formulation for shape optimization using the Navier–Stokes equations has been recently developed by the authors. While a complete description of the method which is presented in reference [1] is beyond the scope of this paper, it is helpful to summarize the general abstract description of the adjoint approach and outline the steps needed for implementing it. It will become clear the role played by efficient viscous solvers in the context of design optimization.

The progress of the design procedure is measured in terms of a cost function I , which could be, for example the drag coefficient or the lift to drag ratio. For flow about an airfoil or wing, the aerodynamic properties which define the cost function are functions of the flow-field variables (w) and the physical location of the boundary, which may be represented by the function \mathcal{F} , say. Then

$$I = I(w, \mathcal{F}),$$

and a change in \mathcal{F} results in a change

$$\delta I = \left[\frac{\partial I^T}{\partial w} \right]_I \delta w + \left[\frac{\partial I^T}{\partial \mathcal{F}} \right]_{II} \delta \mathcal{F}, \quad (27)$$

in the cost function. Here, the subscripts I and II are used to distinguish the contributions due to the variation δw in the flow solution from the change associated directly with the modification $\delta \mathcal{F}$ in the shape. This notation is introduced to assist in grouping the numerous terms that arise during the derivation of the full Navier–Stokes adjoint operator, so that it remains feasible to recognize the

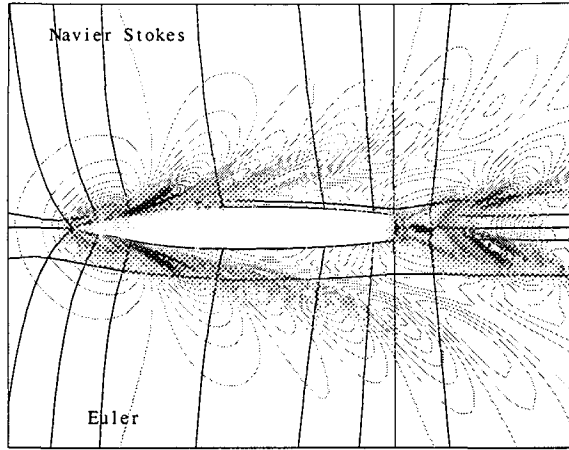


Figure 15: Overhead Wave Profiles: 5415 (Fr = .2756)

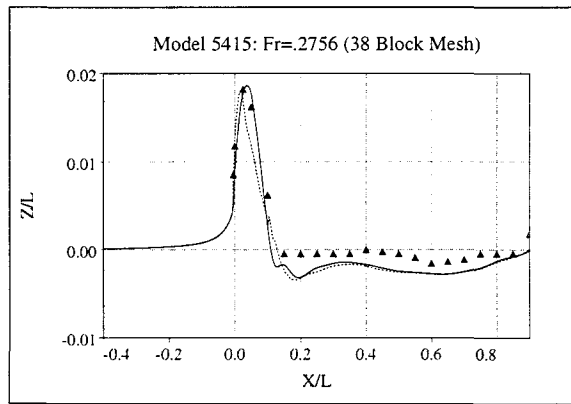


Figure 16: Waterline Comparison: 5415 (Fr = .2756)

basic structure of the approach as it is sketched in the present section.

Using control theory, the governing equations of the flow field are introduced as a constraint in such a way that the final expression for the gradient does not require multiple flow solutions. This corresponds to eliminating δw from (27).

Suppose that the governing equation R which expresses the dependence of w and \mathcal{F} within the flow-field domain \mathcal{D} can be written as

$$R(w, \mathcal{F}) = 0. \quad (28)$$

Then δw is determined from the equation

$$\delta R = \left[\frac{\partial R}{\partial w} \right]_I \delta w + \left[\frac{\partial R}{\partial \mathcal{F}} \right]_{II} \delta \mathcal{F} = 0. \quad (29)$$

Next, introducing a Lagrange Multiplier ψ , we have

$$\begin{aligned} \delta I &= \frac{\partial I^T}{\partial w} \delta w + \frac{\partial I^T}{\partial \mathcal{F}} \delta \mathcal{F} - \psi^T \left(\left[\frac{\partial R}{\partial w} \right] \delta w + \left[\frac{\partial R}{\partial \mathcal{F}} \right] \delta \mathcal{F} \right) \\ &= \left\{ \frac{\partial I^T}{\partial w} - \psi^T \left[\frac{\partial R}{\partial w} \right] \right\}_I \delta w + \left\{ \frac{\partial I^T}{\partial \mathcal{F}} - \psi^T \left[\frac{\partial R}{\partial \mathcal{F}} \right] \right\}_{II} \delta \mathcal{F} \quad (30) \end{aligned}$$

Choosing ψ to satisfy the adjoint equation

$$\left[\frac{\partial R}{\partial w} \right]^T \psi = \frac{\partial I}{\partial w} \quad (31)$$

the first term is eliminated, and we find that

$$\delta I = \mathcal{G} \delta \mathcal{F}, \quad (32)$$

where

$$\mathcal{G} = \frac{\partial I^T}{\partial \mathcal{F}} - \psi^T \left[\frac{\partial R}{\partial \mathcal{F}} \right].$$

The advantage is that (32) is independent of δw , with the result that the gradient of I with respect to an arbitrary number of design variables can be determined without the need for additional flow-field evaluations. In the case that (28) is a partial differential equation, the adjoint equation (31) is also a partial differential equation and determination of the appropriate boundary conditions requires careful mathematical treatment.

The computational cost of a single design cycle is roughly equivalent to the cost of two flow solutions since the the adjoint problem has similar complexity. When the number of design variables becomes large, the computational efficiency of the control theory approach over traditional approach, which requires direct evaluation of the gradients by individually varying each design variable and recomputing the flow field, becomes compelling.

Once equation (29) is established, an improvement can be made with a shape change

$$\delta \mathcal{F} = -\lambda \mathcal{G}$$

where λ is positive, and small enough that the first variation is an accurate estimate of δI . The variation in the cost function then becomes

$$\delta I = -\lambda \mathcal{G}^T \mathcal{G} < 0.$$

After making such a modification, the flow field and corresponding gradient can be recalculated and the process repeated to follow a path of steepest descent until a minimum is reached. In order to avoid violating constraints, such as a minimum acceptable wing thickness, the gradient may be projected into an allowable subspace within which the constraints are satisfied. In this way, procedures can be devised which must necessarily converge at least to a local minimum.

The design procedures using the RANS can be summarized as follows:

1. Solve the flow equations for ρ, u_1, u_2, u_3, p .

2. Solve the adjoint equations for ψ subject to appropriate boundary conditions.
3. Evaluate \mathcal{G} .
4. Project \mathcal{G} into an allowable subspace that satisfies any geometric constraints.
5. Update the shape based on the direction of steepest descent.
6. Return to 1 until convergence is reached.

Thus, practical implementation of the viscous design method relies heavily upon fast and accurate solvers for both the state (w) and co-state (ψ) systems.

A typical result of drag minimization in transonic viscous flow is presented next. This calculation is a redesign of a wing using the viscous adjoint optimization method with a Baldwin-Lomax turbulence model. The initial wing is similar to one produced during the MDXX design studies. Figure 17 show the result of the wing-body redesign on a C-H mesh with $288 \times 96 \times 64$ cells. The wing has sweep back of about 38 degrees at the 1/4 chord. A total of 44 iterations of the viscous optimization procedure resulted in a shock-free wing at a cruise design point of Mach 0.86, with a lift coefficient of 0.61 for the wing-body combination at a Reynolds number of 101 million based on the root chord. Overnight turnaround time is possible on the current generation of parallel computers.

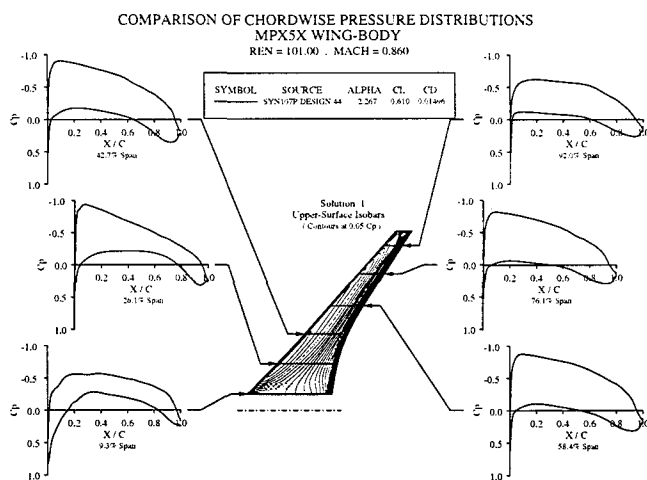


Figure 17: Pressure distribution of the final MPX5X design.

TIME RESOLVED ANALYSIS

Time dependent calculations are needed for a number of important applications, such as flutter analysis or the simulation of the flow past a helicopter rotor, in which the stability limit of an explicit scheme

forces the use of much smaller time steps than would be needed for an accurate simulation. In this situation a multigrid explicit scheme can be used in an inner iteration to drive the solution of a fully implicit time discretization [52].

Suppose that (25) is approximated as

$$D_t w^{n+1} + R(w^{n+1}) = 0.$$

Here D_t is a k^{th} order accurate backwards difference operator of the form

$$D_t = \frac{1}{\Delta t} \sum_{q=1}^k \frac{1}{q} (\Delta^-)^q,$$

where

$$\Delta^- w^{n+1} = w^{n+1} - w^n.$$

Applied to the linear differential equation

$$\frac{dw}{dt} = \alpha w,$$

the schemes with $k = 1, 2$ are stable for all $\alpha \Delta t$ in the left half plane (A-stable). Dahlquist has shown that A-stable linear multi-step schemes are at best second order accurate [53]. Gear however, has shown that the schemes with $k \leq 6$ are stiffly stable [54], and one of the higher order schemes may offer a better compromise between accuracy and stability depending on the application.

Equation (25) is now treated as a modified steady-state problem to be solved by a multigrid scheme using variable local time steps in a fictitious time t^* . For example, in the case $k = 2$ one solves

$$\frac{\partial w}{\partial t^*} = R^*(w),$$

where

$$R^*(w) = \frac{3}{2\Delta t} w + R(w) + \frac{2}{\Delta t} w^n - \frac{1}{2\Delta t} w^{n-1},$$

and the last two terms are treated as fixed source terms. The first term shifts the Fourier symbol of the equivalent model problem to the left in the complex plane. While this promotes stability, it may also require a limit to be imposed on the magnitude of the local time step Δt^* relative to that of the implicit time step Δt . This limitation may be relieved by a point-implicit modification of the multi-stage scheme [55]. In the case of problems with moving boundaries the equations must be modified to allow for movement and deformation of the mesh.

Pitching NACA 64A010 Airfoil

The two dimensional turbulent flow over this airfoil has been calculated using the dual time stepping approach, and the unsteady C_l vs. α curve was found

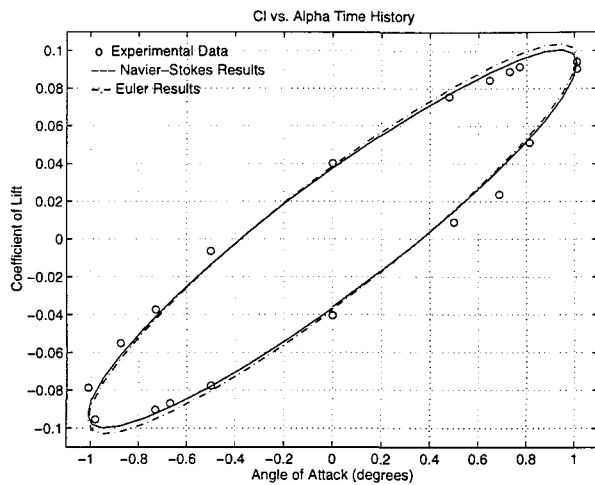


Figure 18: Coefficient of Lift Time History.

to agree quite well with the experiment. The experimental results lie on a periodic curve in the shape of an oval, which is slightly broader than the inviscid calculations. In Figure 18 we can see that the inclusion of viscous effects tilts the inviscid oval in the direction of the experimental results. The very slight difference still existing may be due to inaccuracies in the turbulence model.

However, if in addition one wants to obtain drag and pitching moment information, the only option is to use the full Navier-Stokes equations with a suitable turbulence model. Figure 19 shows the motion of the shocks in the upper and lower surfaces of the airfoil for a little more than half a pitching cycle. The snapshots are arranged by rows. As the airfoil pitches up, the shock in the upper surface moves aft at the same time as it becomes stronger. The shock in the lower surface moves forward, weakens, and disappears. As the airfoil pitches down, the opposite begins to happen, with a small phase lag. By virtue of the use of the H-CUSP, shocks can be resolved very crisply, with the additional advantage that the actual viscosity in the flow field is contaminated to a much lesser degree. Finally, Figure 20 shows the coefficient of pressure along a coordinate line that circles the airfoil right outside of the boundary layer. One can clearly see that these the results, which were obtained with the H-CUSP scheme, are superior to those that could be obtained with a scalar dissipation model which spreads the shock over 4 or 5 cells instead of 1 or 2.

Rigid Rotor-Navier-Stokes Hover

Efficient simulation of the turbulent time dependent flow on rotors is becoming feasible with the current generation of parallel computers, not only in hover

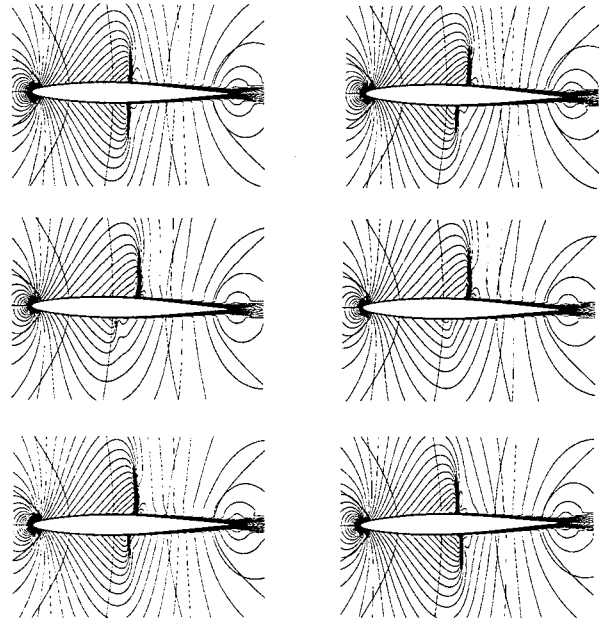


Figure 19: Mach Number Contours. Pitching Airfoil Case. $Re = 1.0 \times 10^6$, $M_\infty = 0.796$, $K_c = 0.202$.

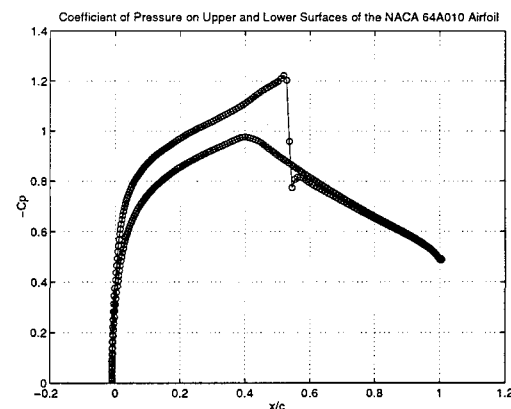


Figure 20: Coefficient of Pressure on a Grid Line at Edge of the Boundary Layer.

but also in forward flight [56]. A Navier-Stokes calculation was performed on the Caradonna rotor [57] at a collective pitch, θ_c , of 8 degrees and a tip Mach number, M_t , of 0.877. Shock-free cases including viscous effects produced results that were very similar to the inviscid and experimental results and are not reproduced here. The grid used in this case was an H-H grid with $256 \times 64 \times 64$ cells, with 128 cells on the surface of the airfoil in the chordwise direction and 48 cells in the spanwise direction. A Baldwin-Lomax turbulence model was used for a tip chord Reynolds number of 3,930,000. Approximately 24 cells lie in the boundary layer of the rotor. This level of resolution has been shown to be satisfactory for these types of calculations when using a CUSP scheme [4, 58]. Figure 21 shows experimental and numerical pressure coefficient distributions at different outboard radial locations of the blade. The most likely causes for this disagreement with experimental measurements are the inadequacy of the Baldwin-Lomax turbulence model for flow cases which include shock-boundary layer interaction such as the present case, and the differences between transition locations in the computation and experiment. Transition in this calculation was fixed at the leading edge of the blade, which may not correspond to the experimental location of transition (which was not specified in the experimental report). To reach an adequate level of convergence (five orders of magnitude reduction in the RMS residual of density), this calculation required 6.5 hours on 16 processors of an IBM SP. The computation was perfectly load balanced with 64 blocks of $32 \times 32 \times 16$ cells.

Vortex Shedding from a Circular Cylinder

The multigrid dual time stepping approach described is easily extended to incompressible flow by using an artificial compressibility approach in the inner iteration. This method, which could be very effective for simulating maneuvering of both surface and submerged ships, has been extensively validated by A. Belov [59] for several benchmark problems.

Flow past a circular cylinder is one of the classical problems in fluid dynamics encompassing, at different Reynolds numbers, a wide variety of fascinating fluid phenomena – from parallel vortex shedding and famous von Kármán vortex street ($Re \geq 50$) to an aerodynamic drag crisis ($Re \sim 5 \times 10^5$). A comprehensive amount of experimental and numerical evidence accumulated for this problem places it among the most valuable benchmarks used in CFD for testing and comparing numerical approaches. At low Reynolds numbers, several vortex shedding phenomena have been accurately captured using our two-dimensional flow solver, as explained in references [60], [59]. These include transition of the flow

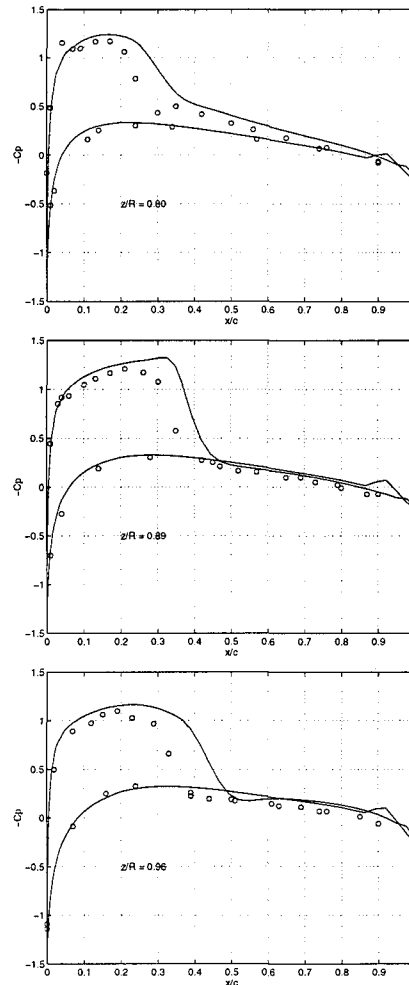


Figure 21: Pressure distribution on a rotor in hover, $\theta_c = 8^\circ$, $M_t = 0.877$.

to the unsteady regime at $47 < Re_c < 48$ and the spanwise independent, so called “parallel” shedding regime [61] at $50 \leq Re \leq 180$.

According to reference [61], above $Re \sim 180$ the flow becomes three-dimensional and exhibits spanwise vortex loops with a spanwise length scale of about 3 diameters (shedding mode “A”). The transition to three-dimensionality is subcritical [62] and is marked by a discontinuous drop in the Strouhal frequency

The exact reason for this reduction in St is still not fully understood and may be attributed to either primary vortex deformations or to the spot-like “vortex dislocations”, described in references [63], [64]. A second discontinuity in the $St(Re)$ curve occurs at $Re = 230 - 260$, when the aforementioned vortex loops give way to a finer scale vortex structure (shedding mode “B”), described in detail in references [61], [63]. It is important to note that the double value region of the $St(Re)$ curve corresponding to this transition is *not hysteretic* but reflects temporal intermittency between the two modes A

	Grid 128x128	Grid 96x64x32	
	2-D Shedding	Initial 2-D	3-D
Cl	± 0.703	± 0.701	Modulated
Cd_{max}	1.26	1.27	1.20
Cpb	-1.00	-1.02	-0.855
St	0.201	0.205	0.186

Table 1: Comparison of the 2-D and 3-D results, $Re=225$.

and B [61].

To investigate this transition, three-dimensional computations at Reynolds numbers 150, 225 and 250 were performed on a O-H-mesh using $96 \times 64 \times 32$ cells with the far field boundary extended 25 diameters from the center of the cylinder. The aspect ratio of a cylinder is $L/D = 6.4$.

An initial disturbance is introduced in the flow to expedite the onset of the shedding. The disturbance imitates the distributed torsion deformation of a cylinder: spanwise sections of a cylinder are rotated in their planes with a common frequency but with a random amplitude between 0° and 5° degrees and then stopped. The spanwise variation of the base pressure coefficient $d(Cpb) = Cpb_{max} - Cpb_{min}$ is considered as one of the indicators of three-dimensionality. Its time history is shown in Figure 22 for $Re = 150$ and $Re = 225$. The re-

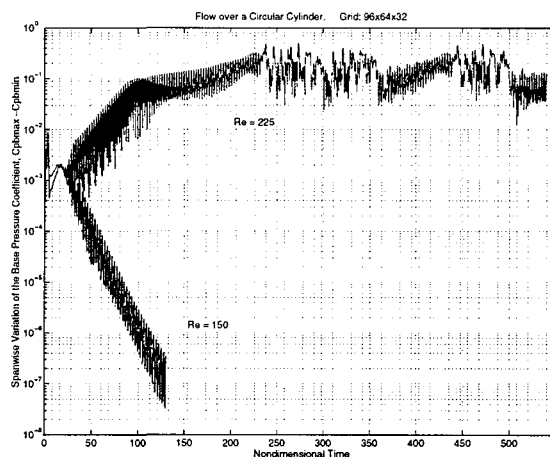


Figure 22: Disturbance Evolution as Measured by the Spanwise Variation of Base Pressure Coefficient $dCpb(t)$. Three-Dimensional Flow around Circular Cylinder, $Re=150$ and $Re=225$.

sults for $Re = 150$ exhibit a decaying response to the initial disturbance and reach, asymptotically, a two-dimensional shedding, which is in agreement with the experimental predictions. At $Re = 225$ the flow is unstable to the same disturbance: ini-

tially the flow develops essentially two-dimensional shedding, and then, the $d(Cpb)$ and the maximum spanwise velocity component gradually increase by two orders in magnitude until the fully evolved 3-D shedding results. The time-averaged flow quantities corresponding to the initial parallel shedding regime agree reasonably well with those computed by the two-dimensional solver, as compared in Table 1, given the difference in spatial resolution of the two meshes. The time evolution of the lift coefficient for the $Re = 225$ case is shown in Figure 23. The onset of the three-dimensionality is marked by

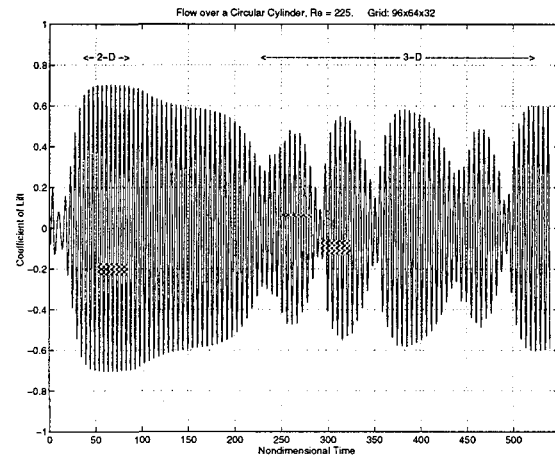


Figure 23: Three-Dimensional Flow over a Circular Cylinder. Evolution of the Lift Coefficient.

a sharp reduction in the lift coefficient, the Strouhal frequency and the base suction ($-Cpb$). This is similar to the results of a computation with $Re = 525$, described in reference [65]. A pronounced modulation of the lift coefficient is observed in Figure 23, presumably indicating the formation of vortices with varying degrees of coherence along the spanwise direction. Also, not only the Cl amplitude, but also the shedding period itself were found to vary with time. This suggests that a single St frequency description is inadequate for this flow regime and possibly explains the double value region in the experimental $St(Re)$ curve [61]. These findings are in line with experimental observations [64] and can be potentially explained by the vortex dislocation mechanism [63]. Nevertheless, higher aspect ratio and better resolved computations may be necessary to investigate this phenomenon. One can observe two distinctive patterns in time histories of $d(Cpb)$ and the Cl , superimposed in Figure 24. The correlation of $d(Cpb)$ with Cl seems to suggest an intermittency between two distinctive shedding modes. A “coherent” C-mode, defined by high Cl and regular small-amplitude $d(Cpb)$ variations, corresponds to essentially two-dimensional flow behavior next to

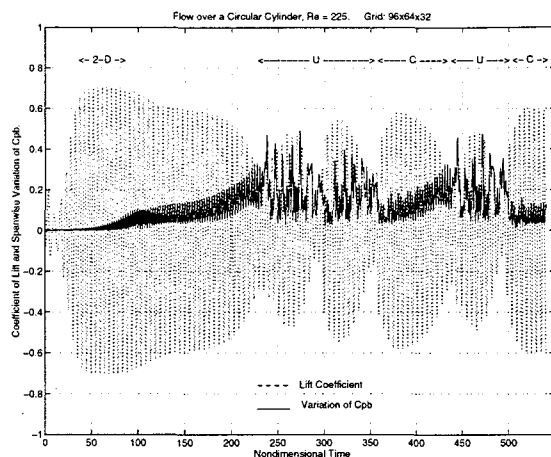


Figure 24: Superimposed Time Evolution of Cl and $d(Cpb)$, $Re=225$.

the cylinder. By contrast, low Cl and sporadic large-amplitude excursions of $d(Cpb)$ (“uncorrelated” U-mode) reveal a highly three-dimensional vortex formation region next to the cylinder’s surface. Thus, the region where transition to three-dimensionality occurs migrates continuously up- and downstream between the cylinder and the near wake. This finding may explain the Cl modulation, the accompanying temporal variation of the shedding period and the double value region of the $St(Re)$ curve observed in the experiments.

Time-averaged results for the three-dimensional shedding mode for Reynolds numbers 225 and 250 agrees quite well with the lower branches of the experimental data curves corresponding to the shedding mode “A” as defined in references [61], [63]. According to this source, the “A” mode of vortex shedding is characterized by the presence of the streamwise vortex loops with a spanwise wavelength of about 3 diameters. Similar structures are also observed in our calculations.

CONCLUSIONS

Following a development that lasted approximately fifteen years, viscous solvers based on finite volume discretizations and multigrid time stepping are now well established. The theoretical underpinning of these methods is by enlarge well understood, and sophisticated implementations are available. Thus, it is entirely feasible to conduct three dimensional viscous analyses of complete configurations.

The current generation of parallel computers enables a cost effective solution of viscous problems which bear a computational costs equivalent to multiple

steady state solutions. These include chemically reactive flows with detailed chemistry models, design optimization, and time accurate simulation of three dimensional flow. As the power of microprocessors continues to increase, it will become possible for industry to make an effective use of viscous simulation at an early stage of the design.

Improvements in asymptotic convergence rate are still possible and desirable. They may be achieved using preconditioning techniques and improved multigrid strategies. At present, however, these techniques appear to be very sensitive to the quality of the mesh, and more research is needed before these methods become suitable for industrial use.

ACKNOWLEDGEMENT

This work has benefited from the generous support of AFOSR under Grant No. AFOSR-91-0391, the NASA-IBM Cooperative Research Agreement, and continuous support of the Office of Naval Research.

REFERENCES

- [1] A. Jameson, L. Martinelli, and N. A. Pierce. Optimum aerodynamic design using the Navier-Stokes equations. *Theoret. Comput. Fluid Dynamics*, 10:213–237, 1998.
- [2] A. Jameson, J. J. Alonso, , J. Reuther, J. C. Vassberg, , and L. Martinelli. Aerodynamic shape optimization techniques based on control theory. *AIAA paper 98-2538*, June 1998.
- [3] A. Jameson. Computational algorithms for aerodynamic analysis and design. *Appl. Num. Math.*, 13:383–422, 1993.
- [4] S. Tatsumi, L. Martinelli, and A. Jameson. Design, implementation, and validation of flux limited schemes for the solution of the compressible Navier-Stokes equations. *AIAA paper 94-0647*, AIAA 32nd Aerospace Sciences Meeting, Reno, Nevada, January 1994.
- [5] S. Tatsumi, L. Martinelli, and A. Jameson. A new high resolution scheme for compressible viscous flows with shocks. *AIAA paper To Appear*, AIAA 33nd Aerospace Sciences Meeting, Reno, Nevada, January 1995.
- [6] P.L. Roe. Fluctuations and signals - a framework for numerical evolution problems. In K.W. Morton and M.J. Baines, editors, *Proceedings of IMA Conference on Numerical Methods in Fluid Dynamics*, pages 219–257, Reading, 1981.
- [7] A. Jameson. Analysis and design of numerical schemes for gas dynamics 2, artificial diffusion

- and discrete shock structure. *Int. J. of Comp. Fluid Dyn.*, To Appear.
- [8] M-S. Liou and C.J. Steffen. A new flux splitting scheme. *J. Comp. Phys.*, 107:23-39, 1993.
- [9] Y. Wada and M-S. Liou. A flux splitting scheme with high-resolution and robustness for discontinuities. *AIAA paper 94-0083*, AIAA 32nd Aerospace Sciences Meeting, Reno, Nevada, January 1994.
- [10] B. Van Leer. Towards the ultimate conservative difference scheme. II. Monotonicity and conservation combined in a second order scheme. *J. Comp. Phys.*, 14:361-370, 1974.
- [11] A. Jameson. Analysis and design of numerical schemes for gas dynamics I, artificial diffusion, upwind biasing, limiters and their effect on multigrid convergence. *Int. J. of Comp. Fluid Dyn.*, 4:171-218, 1995.
- [12] R. Chipman and A. Jameson. Fully conservative numerical solutions for unsteady irrotational transonic flow about airfoils. AIAA Paper 79-1555, AIAA 12th Fluid and Plasma Dynamics Conference, Williamsburg, VA, July 1979.
- [13] A. Jameson, W. Schmidt, and E. Turkel. Numerical solution of the Euler equations by finite volume methods using Runge-Kutta time stepping schemes. AIAA Paper 81-1259, 1981.
- [14] A. Jameson. Multigrid algorithms for compressible flow calculations. In *Second European Conference on Multigrid Methods*, Cologne, October 1985. Princeton University Report MAE 1743.
- [15] A. Jameson. Transonic flow calculations for aircraft. In F. Brezzi, editor, *Lecture Notes in Mathematics, Numerical Methods in Fluid Dynamics*, pages 156-242. Springer Verlag, 1985.
- [16] A. Rizzi and L.E. Eriksson. Computation of flow around wings based on the Euler equations. *J. Fluid Mech.*, 148:45-71, 1984.
- [17] A. Jameson, T.J. Baker, and N.P. Weatherill. Calculation of inviscid transonic flow over a complete aircraft. *AIAA paper 86-0103*, AIAA 24th Aerospace Sciences Meeting, Reno, Nevada, January 1986.
- [18] L. Martinelli. Calculations of viscous flows with a multigrid method. *Princeton University Thesis*, May 1987.
- [19] R.P. Fedorenko. The speed of convergence of one iterative process. *USSR Comp. Math. and Math. Phys.*, 4:227-235, 1964.
- [20] A. Brandt. Multi-level adaptive solutions to boundary value problems. *Math. Comp.*, 31:333-390, 1977.
- [21] W. Hackbusch. On the multi-grid method applied to difference equations. *Computing*, 20:291-306, 1978.
- [22] R.H. Ni. A multiple grid scheme for solving the Euler equations. *AIAA Journal*, 20:1565-1571, 1982.
- [23] A. Jameson. Solution of the Euler equations by a multigrid method. *Appl. Math. and Comp.*, 13:327-356, 1983.
- [24] M.G. Hall. Cell vertex multigrid schemes for solution of the Euler equations. In *Proc. IMA Conference on Numerical Methods for Fluid Dynamics*, Reading, April 1985.
- [25] A. Jameson. A vertex based multigrid algorithm for three-dimensional compressible flow calculations. In T.E. Tezduar and T.J.R. Hughes, editors, *Numerical Methods for Compressible Flow - Finite Difference, Element And Volume Techniques*, 1986. ASME Publication AMD 78.
- [26] D.A. Caughey. A diagonal implicit multigrid algorithm for the Euler equations. AIAA Paper 87-453, 25th Aerospace Sciences Meeting, Reno, January 1987.
- [27] W.K. Anderson, J.L. Thomas, and D.L. Whitfield. Multigrid acceleration of the flux split Euler equations. AIAA Paper 86-0274, AIAA 24th Aerospace Sciences Meeting, Reno, January 1986.
- [28] P.W. Hemker and S.P. Spekreijse. Multigrid solution of the steady Euler equations. In *Proc. Oberwolfach Meeting on Multigrid Methods*, December 1984.
- [29] A. Jameson and D.J. Mavriplis. Multigrid solution of the Euler equations on unstructured and adaptive grids. In S. McCormick, editor, *Multigrid Methods, Theory, Applications and Supercomputing. Lecture Notes in Pure and Applied Mathematics*, volume 110, pages 413-430, April 1987.
- [30] M.H. Lallemand and A. Dervieux. A multigrid finite-element method for solving the two-dimensional Euler equations. In S.F. McCormick, editor, *Proceedings of the Third Copper Mountain Conference on Multigrid Methods, Lecture Notes in Pure and Applied Mathematics*, pages 337-363, Copper Mountain, April 1987.

- [31] Allmaras S.R. Algebraic smoothing analysis of multigrid methods for the 2-d compressible Navier-Stokes equation. *AIAA Paper 97-1954*, 13th Computational Fluid Dynamics Conference AIAA, Snowmass, Co, 1997.
- [32] N.A. Pierce and M.B. Giles. Preconditioning compressible flow calculations on stretched meshes. *AIAA Paper 96-0889*, 34th Aerospace Sciences Meeting and Exhibit, Reno, NV, 1996.
- [33] N.A. Pierce, M.B. Giles, A. Jameson, and L. Martinelli. Accelerating three-dimensional Navier-Stokes calculations.
- [34] V. Venkatakrishnan. Improved multigrid performance of Navier-Stokes solvers. *AIAA paper 98-2967*, 29th Fluid Dynamics Conference, Albuquerque, NM, June 1998.
- [35] D. Mavriplis. On convergence acceleration techniques for unstructured mesh solvers. *AIAA paper 98-2966*, 29th Fluid Dynamics Conference, Albuquerque, NM, June 1998.
- [36] A. Jameson and J.J. Alonso. Automatic aerodynamic optimization on distributed memory architectures. *AIAA paper 96-0409*, 34th Aerospace Sciences Meeting and Exhibit, Reno, Nevada, January 1996.
- [37] J. J. Alonso, T. J. Mitty, L. Martinelli, and A. Jameson. A two-dimensional multigrid-driven Navier-Stokes solver for multiprocessor architectures. In *Proceedings of the Parallel CFD '94 Conference*, Kyoto, Japan, May 1994.
- [38] A. Elsenaar and H.W.M. Hoeijmakers. An experimental study of the flow over a sharp leading edge cropped delta wing at subsonic, transonic and supersonic speed. NLR TP-91117L, 1991.
- [39] S. G. Sheffer. *Parallel Computation of Supersonic Reactive Flows with Detailed Chemistry Including Viscous and Species Diffusion Effects*. PhD thesis, Princeton University, Department of Mechanical and Aerospace Engineering, June 1997.
- [40] J. S. Evans and C. J. Schexnayder. Influence of chemical kinetics and unmixedness on burning in supersonic hydrogen flames. *AIAA Journal*, 18(2):180-193, February 1980.
- [41] H. F. Lehr. Experiments on shock-induced combustion. *Astronautica Acta*, 17:589-596, 1972.
- [42] S. Yungster, S. Eberhardt, and A. P. Bruckner. Numerical simulation of hypervelocity projectiles in detonable gases. *AIAA Journal*, 29(2):187-199, February 1991.
- [43] T. Chitsomboon, A. Kumar, and S. N. Tiwari. Numerical study of finite-rate supersonic combustion using parabolized equations. *AIAA paper 87-0088*, AIAA 25th Aerospace Sciences Meeting and Exhibit, Reno, NV, January 1987.
- [44] H. C. Yee and J. L. Shinn. Semi-implicit and fully implicit shock-capturing methods for nonequilibrium flows. *AIAA Journal*, 27(3):299-307, March 1989.
- [45] J. S. Shuen and S. Yoon. Numerical study of chemically reacting flows using a lower-upper symmetric successive overrelaxation scheme. *AIAA Journal*, 27(12):1752-1760, December 1989.
- [46] Y. Ju. Lower-upper scheme for chemically reacting flow with finite rate chemistry. *AIAA Journal*, 33(8):1418-1425, August 1995.
- [47] Farmer J.R., Martinelli L., and Jameson A. A fast multigrid method for solving the nonlinear ship wave problem with a free surface.
- [48] Farmer J.R., Martinelli L., and Jameson A. A fast multigrid method for solving incompressible hydrodynamic problems with free surfaces. *AIAA Journal*, 32 no. 6:1175-1182, 1994.
- [49] Chorin A. A numerical method for solving incompressible viscous flow problems. *Journal of Computational Physics*, 2:12-26, 1967.
- [50] A. Rizzi and L.E. Eriksson. Computation of inviscid incompressible flow with rotation. *J. Fluid Mech.*, 153:275-312, 1985.
- [51] Y. Toda, F. Stern, and J. Longo.
- [52] A. Jameson. Time dependent calculations using multigrid, with applications to unsteady flows past airfoils and wings. *AIAA paper 91-1596*, AIAA 10th Computational Fluid Dynamics Conference, Honolulu, Hawaii, June 1991.
- [53] G. Dahlquist. A special stability problem for linear multistep methods. *BIT*, 3:27-43, 1963.
- [54] C.W. Gear. The numerical integration of stiff ordinary differential equations. Report 221, University of Illinois Department of Computer Science, 1967.
- [55] N. D. Melson, M. D. Sanetrik, and H. L. Atkins. Time-accurate Navier-Stokes calculations with multigrid acceleration. In *Proceedings of the Sixth Copper Mountain Conference on Multigrid Methods*, Copper Mountain, April 1993.
- [56] S. G. Sheffer, J. J. Alonso, L. Martinelli, and A. Jameson. Time-accurate simulation of helicopter rotor flows including aeroelastic effects.

AIAA paper 97-0399, AIAA 35th Aerospace Sciences Meeting and Exhibit, Reno, NV, January 6-9 1997.

- [57] F. X. Caradonna and C. Tung. Experimental and analytical studies of a model helicopter rotor in hover. NASA TM 81232, AVRADCOM Research and Technology Laboratories, 1981.
- [58] J. J. Alonso, L. Martinelli, and A. Jameson. Multigrid unsteady Navier-Stokes calculations with aeroelastic applications. *AIAA paper 95-0048*, AIAA 33rd Aerospace Sciences Meeting, Reno, Nevada, January 1995.
- [59] A. A. Belov. *A New Implicit Multigrid-Driven Algorithm for Unsteady Incompressible Flow Calculations on Parallel Computers*. PhD thesis, Princeton University, Department of Mechanical and Aerospace Engineering, June 1997.
- [60] A. Belov, L. Martinelli, and A. Jameson. A new implicit algorithm with multigrid for unsteady incompressible flow calculations. *AIAA paper 95-0049*, AIAA 33rd Aerospace Sciences Meeting, Reno, Nevada, January 1995.
- [61] C.H.K. Williamson and A. Roshko. Measurements of base pressure in the wake of a cylinder at low Reynolds numbers number relationship for the laminar vortex shedding. *Z. Flugwiss. Weltraumforsch.*, 14:38-46, 1990.
- [62] R. D. Henderson and D. Barkley. Secondary instability in the wake of a circular cylinder. *Phys. Fluids*, 8(6):pp. 1683-1685, 1996.
- [63] C. H. K. Williamson. The natural and forced formation of spot-like "vortex dislocations" in the transition of a wake. *J. Fluid Mech.*, 243:pp. 393-441, 1992.
- [64] C. H. K. Williamson. American Physical Society Meeting, November 1996. Private communication.
- [65] S. Balachandar and R. Mittal. Momentum and vorticity transport by 3-d vortical structures in bluff body wakes. In *The 10th Symposium on Turbulent Shear Flows*, volume 1 of 4, pages pp. 4-7. The Pennsylvania State University, 1995.